BRIEF REPORT

Iterative immunostaining combined with expansion microscopy and image processing reveals nanoscopic network organization of nuclear lamina

Elina Mäntylä,[a*] Toni Montonen,[a*] Lucio Azzari,[b] Salla Mattola,[c] Markus Hannula,[a] Maija Vihinen-Ranta,[c] Jari Hyttinen,[a] Minnamari Vippola,[d] Alessandro Foi,[e] Soile Nymark,[a] Teemu O. Ihalainen[a]

BioMediTech, Faculty of Medicine and Health Technology, Tampere University, Tampere, Finland[a]; Faculty of Engineering and Natural Sciences, Materials Science and Environmental Engineering, Tampere University, Tampere, Finland[b]; Department of Biological and Environmental Science and Nanoscience Center, University of Jyväskylä, Jyväskylä, Finland[c]; Faculty of Engineering and Natural Sciences, Materials Science and Environmental Engineering, Engineering Materials Science, Tampere University, Tampere, Finland,[d]; Faculty of Information Technology and Communication Sciences, Computing Sciences, Tampere University, Tampere, Finland[e]

#Address correspondence to Teemu Ihalainen, teemu.ihalainen@tuni.fi
*Equal contribution

Address: BioMediTech, Faculty of Medicine and Health Technology, Tampere, University, Tampere, Finland. Arvo Ylpön katu 34, 33520 Tampere, Finland
Phone: +358 50 3187 202

Characters (without spaces): 21 509
Running head: IT-IF IN EXPANSION MICROSCOPY OF LAMINS

Abbreviations:

ExM	Expansion microscopy
FWHM	Full width at half maximum
HSV-1	Herpes simplex virus 1

IT-IF	Iterative indirect immunofluorescence staining
LA/C-C	Lamin A/C C-terminus
LA/C-N	Lamin A/C N-terminus
LA/C-rod	Lamin A/C rod-domain
NE	Nuclear envelope
PAA	Polyacrylamide
SBR	Signal-to-background -ratio
SIM	Structured illumination microscopy
SR-SIM	Super-resolution structured illumination microscopy

Abstract

Investigation of nuclear lamina architecture relies on super-resolved microscopy. However, epitope accessibility, labeling density, and detection precision of individual molecules poses challenges within the molecularly crowded nucleus. We developed an iterative indirect immunofluorescence staining (IT–IF) approach combined with expansion microscopy (ExM) and structured illumination microscopy (SIM) improving super-resolution microscopy of subnuclear nanostructures like nuclear lamina. First, we prove that ExM is applicable in analyzing structurally highly compacted nuclear multiprotein complexes such as viral nucleocapsids. Second, we provide technical improvements to the ExM method, including 3D-printed gel casting equipment. Third, show that in comparison to conventional immunostaining, iterative labeling of intranuclear targets like nuclear lamina results in a higher signal-to-background –ratio (SBR) and mean fluorescence intensity and use structured illumination microscopy and ExM to critically point out that iterative immunostaining results in improved target labeling density, benefiting the structural analyses via ExM. Lastly, we develop a signal processing pipeline for noise estimation, denoising and deblurring in analysis of lamin network and provide this platform to the microscopy imaging research community. Our work reveals the potential of signal-resolved IT–IF in super-resolution imaging of lamin network organization — a prerequisite for studying intranuclear structural co-regulation of cell function and fate. (Words: 197)

Introduction

Nuclear envelope (NE) is underlined by a tight proteinaceous network called the nuclear lamina. The nuclear lamina is formed from A- and B-type lamins of the type V intermediate filament protein family, and lamin-associated proteins (Schirmer *et al.*, 2003). The A- and B-

type lamins form separate layers with the latter situated closer to the inner nuclear membrane than the A-type lamins (Figueiras *et al.*, 2019). Together, this nuclear lamin meshwork is approximately a 14 nm-thick layer being less than one-tenth of the resolution of diffraction-limited fluorescence microscopy (Pawley, 2006). The nuclear lamina is necessary for the mechanical stability of the nucleus (Dahl *et al.*, 2004) and responds to mechanical cues (Ankam *et al.*, 2018). It has a pivotal role in regulating genome organization and gene expression (Brueckner *et al.*, 2020) by tethering heterochromatin to the NE (Robson *et al.*, 2016). The nuclear lamina –chromatin interaction is highly dynamic (Dixon *et al.*, 2015), and has been reported to change, e.g., during differentiation (Cavalli and Misteli, 2013; Fortin and Hansen, 2015). To study the role of lamins in co-regulation of the genome, detailed understanding of the structural organization of the nuclear lamina is required. Hence, super-resolution imaging of the nuclear lamina has gained significant interest.

Expansion microscopy (ExM) is a tempting super-resolution microscopy technique enabling detection of complex nanostructures by using fluorescence-based imaging modalities, e.g., selective plane illumination microscopy (SPIM) or laser scanning confocal microscopy (LSCM). ExM is based on isotropic enlargement of the sample via 4X – 10X expandable hydrogel. However, this expansion also dilutes the fluorescent molecules in the sample, greatly reducing the resulting image brightness. The dilution scales to the third power of the (linear) expansion factor and thus even 4X expansion can lead to a 64X reduction of the fluorescent signal. To compensate for the dilution, high-quality imaging with ExM, as with other super-resolution methods, requires high-density labeling of the targets of interest (Dankovich and Rizzoli, 2021). However, conventional indirect immunostaining can be insufficient and include non-specific binding, which causes off-target staining of the background and the consequent reduction of the image signal-to-background ratio (SBR) and contrast (Lau *et al.*, 2012; Whelan and Bell, 2015). Furthermore, the accessibility of the target protein epitopes can drastically affect the quality of the data (Schnell *et al.*, 2012) The low signal-to-noise ratio (SNR) in ExM can be improved by post-processing the data, by denoising (Chen *et al.*, 2021), deconvolution (Ikoma *et al.*, 2018), or by a combination of both.

We present improved ExM complemented with iterative immunofluorescence staining, optimized for super-resolution imaging of highly compact intranuclear structures. The iterative labeling greatly increases the intensity of the labeling, without substantially affecting the SBR. In addition, we provide free image processing tools specifically designed to perform noise reduction on LSCM data, which further improves the detection of structural details of the

nuclear lamina network facilitating quantitative analysis of nuclear lamina composition and interactions.

Results and discussion

ExM enables high-resolution imaging of highly compacted nuclear multiprotein complexes but compromises fluorescence intensity and signal-to-background -ratio

ExM allows super-resolution imaging of biological specimens using standard fluorescence microscopy systems. It is based on the isotropic physical expansion of the sample, leading to a corresponding increase in spatial resolution (Tillberg *et al.*, 2016). In this method, fixed and immunostained samples are treated with a cross-linker, embedded into polyacrylamide (PAA) hydrogel, homogenized, and osmotically expanded in water (Figure 1A). Here, we investigated if ExM results in isotropic expansion of rigid and compact nano-scale structures within the nucleus. For this HSV-1 -infected fibroblasts (12 h post infection, multiplicity of infection 5) were used (Figure 1B). HSV-1 naturally targets nuclei for replication and 125 nm -wide progeny capsids are produced and self-assembled in nucleoplasm (Newcomb *et al.*, 1996; Ojala *et al.*, 2000; Baines, 2011). After immunostaining with viral capsid protein 5 (VP5) Ab, the samples were prepared for ExM as described above (n=2, expansion factor ~4), imaged with LSCM and deconvoluted. From images 12 intranuclear anti-VP5 labeled ring-like viral nucleocapsids were extracted, aligned, averaged, and their mean diameter was measured as the peak-to-peak distance from the normalized intensity profile. The mean capsid size was 125.4 nm correlating well with that of the native virus (Figure 1B). This is in good agreement with previous studies, where super-resolution STORM-imaging of HSV-1 resulted approximately 133 nm diameter for the tegument layer outside the capsid (Laine *et al.*, 2015). Thus, the assay showed successful isotropic expansion of the viral capsids inside the nucleus, indicating that ExM is well suitable for super-resolution imaging of compact intranuclear objects (Gao *et al.*, 2021).

Next, we compared the performances of LSCM, SR-SIM, and ExM+LSCM in imaging of nuclear lamina (Figure 1C). Previous cryogenic electron microscopy tomography and fluorescence lifetime –based reports on the molecular architecture of the ~14 nm thick nuclear lamina have shown that A- and B-type lamins form separated networks with LA/C layer being ~10 nm in thicknesses (Turgay *et al.*, 2017; Figueiras *et al.*, 2019). Thus, the nuclear lamina is considerably smaller than the diffraction limited resolution of confocal microscope and presents a good intranuclear target for comparison of different imaging modalities. Here, cells

were immunolabeled with a mouse monoclonal Ab (mMAb) targeting the lamin A/C rod-domain (LA/C-rod) and mounted for high-resolution LSCM and SR-SIM (n=2). Consequently, LA/C-rod -stained ExM samples were prepared from replicate samples by crosslinking and embedding into the PAA gel using novel in-house 3D-printed spacers specifically designed for this study to ensure constant sample gel thickness and diameter (Supplemental Figure 1A and 1B). Following the homogenization, the samples were expanded in water (resulting expansion factor ~4.4). Following imaging with LSCM, SR-SIM, and ExM+LSCM, the width of the LA/C rim was determined from the middle section of the nucleus by measuring the full width at half maximum (FWHM) (Figure 1C). The LSCM yielded the thickest lamina with a mean thickness of 273.0 nm ± 0.04 nm. The SR-SIM improved the resolution, and the lamina thickness was 182.0 nm ± 0.4 nm. ExM provided the highest resolution, with a lamina thickness of 110.0 nm ± 0.4 nm. The results indicate that the ExM yields considerably improved resolution (smaller FWHM of the nuclear lamina) when compared to LSCM or SR-SIM, when imaging intranuclear structures. LSCM and SR-SIM showed surprisingly mediocre performance and the resulting thicknesses were much larger than the theoretical diffraction limit.

Third, Ab concentrations used in ExM are typically higher than those used in conventional immunostaining protocols because the ExM dilutes fluorescence signal by a factor of expansion in the power of three (Truckenbrodt *et al.*, 2019). To demonstrate this effect, pre- and post-expansion samples were prepared from cells stably expressing histone H2B-EGFP. In addition, to visualize the effect of expansion on the Ab -derived intensity, replicate samples were stained with an Ab recognizing LA/C N-terminus (LA/C-N) using standard Ab concentrations. To study the effects of high Ab concentration on the intensity and the SBR, additional samples were prepared with 4X higher primary and secondary Ab concentrations. The fluorescence intensity and the mean signal-to-background ratio (SBR) were determined with identical LSCM imaging settings before and after the expansion (expansion factor 4.4) (n=2). Of note, the SBR described the ratio of background-corrected nuclear intensity to the intensity resulting from off-target and background staining measured from the cytoplasm.

The H2B-EGFP intensity was found to be 1620 ± 140 (a.u.) (mean ± standard deviation) before the expansion but was significantly reduced by 91 % to 153 ± 41 a.u. in expansion. Consequently, the SBR before the expansion was 14.7 but decreased by 88 % to 1.7 after the expansion (Figure 1D and 1E). For LA/C-N, the intensity was 257 ± 53 a.u. before the

expansion, whereas after the expansion it was 183 ± 81 a.u. (n=2) showing that the expansion lead into a ~30 % decrease in the intensity. Consequently, the expansion led to an 58 % decrease in the mean SBR (from SBR of 3.1 to 1.3) (Figure 1E). The analysis of samples containing 4X LA/C-N Ab concentrations showed the intensities were almost 4X higher in comparison to that acquired with 1X concentrations. Specifically, the quantification indicated that the LA/C-N intensity before the expansion was 950 ± 150 a.u. whereas after the expansion it was 435 ± 72 a.u. meaning a 54 % decrease in the intensity following the expansion. However, the expansion led to 71 % decrease in the SBR from 6.6 to 1.9 (Figure 1E).

The results describe the reduction in intensity SBR in ExM imaging demonstrating the ExM decreases signal intensity due to dilution of the fluorophores within the sample (Truckenbrodt *et al.*, 2018; Wassie, Zhao and Boyden, 2019; Gaudreau-Lapierre *et al.*, 2021). The caveat here is that proper imaging of samples like this requires longer acquisition times and higher detector gains leading to increased noise and photobleaching in the sample. Increasing the Ab concentration solely does not rescue the image quality and further highlights the need to increase the signal intensity and SBR in ExM. Together, the results indicate that ExM enables imaging of highly compacted nuclear protein assemblies. However, as our analysis of the pre- and post-ExM gel-embedded samples showed, the labeling method needed to be further developed to counteract the resulting decrease in sample fluorescent intensity and signal quality.

Altered concentration-ratio of primary and secondary Abs does not improve fluorescence signal intensity or signal-to-background ratio

We then sought to study whether sample intensity or SBR could be improved by changing the ratio of primary (1°) or secondary (2°) Abs. For this, we used either traditional (1X) or increased (4X) 1°/2°Ab concentrations while simultaneously using the 1X concentration of the other, respectively (n=2; see also Supplemental Figure 2 for histone H3 Ab).

The analysis of samples stained with traditional 1X concentrations of both 1°Ab (LA/C-N) and 2°Abs and normalized to DAPI signal intensity showed, a mean nuclear fluorescence intensity (± standard deviation, n=2) of 0.6 ± 0.07 a.u. with a mean SBR of 8.6 ± 3.1 (Figure 2A-C). In comparison, using 4X 1° Ab with 1X 2° Ab or 1X 1° Ab with 4X 2° Ab did significantly affect neither the fluorescence intensity (0.6 ± 0.19 and 0.7 ± 0.25 a.u., respectively) nor the mean SBR (6.6 ± 2.7 and 7.1 ± 3.9, respectively) (Figure 2A-C). Comparable results were obtained using histone H3 Ab labeling (Supplemental Figure 2A-F).

To analyze further, the labeling density and efficacy in the concentration-enhanced samples were imaged with SIM (Figure 2D-E) and ExM (Figure 2F-G) (see also Supplemental Figure 2G and 2H for H3 staining). In comparison to the LSCM, SIM produced a more resolved lamin network (Figure 2D-E) highlighting the significance of super-resolution imaging in studying lamins. However, the treatments did not influence the SIM exposure time indicating equal intensities between the samples. Finally, ExM-LSCM imaging revealed that increased concentration of the primary Ab (4X 1° Ab) was required to obtain a better signal (Figure 2F, panel iv). The increase in Ab abundance resulted in more dense staining and visually improved detection of filamentous-like structures within the sample. However, increased background staining was also observed (Figure 2G, panel iv). In comparison, the samples treated with 4X 2° Ab were dim (Figure 2F, panel v), and the labeling density was low (Figure 2G, panel v).

Together, these results showed that increasing the 1° or 2°Ab concentrations alone is insufficient to improve the image quality in SIM and ExM-LSCM. However, increasing the 1° Ab concentration improves the labeling density benefiting ExM-LSCM where fluorophores become diluted during expansion. However, as multiple concentrations were not tested here, it needs to be highlighted that careful optimization of the Ab concentrations should always be considered as the first step to improve the intensity and SBR.

Iterative indirect immunostaining improves fluorescence intensity while preserving a high signal-to-background ratio

To improve the staining process by increased Ab abundance within the sample, iterative indirect immunostaining (IT-IF) was implemented. Here, subsequent immunostaining cycles were performed four times, omitting the blocking step in the last three. Each round involved five steps: i) permeabilization followed by ii) incubation with a 1° Ab targeted against different epitopes in LA/C (see also Supplemental Figure 3 for histone H3, H3K9me3, and fluorophore-conjugated actin phalloidin) and uniquely determined optimal concentrations (referred here as 1X) according to manufacturer´s instructions, iii) washing, and finally iv) 2° Ab incubation using conventional immunostaining and optimized concentrations. LSCM imaging samples were prepared from each cycle.

First, to ensure that the detection conditions did not interfere with the analysis involving weak fluorescence intensities, the effects of detector voltage and laser power on the linearity of the detection were determined (Supplemental Figure 4). For the iteration experiments, the nuclear lamins were stained with either a monoclonal LA/C-N (PFA and MetOH fixed), a

monoclonal LA/C Abs against protein C-terminus LA/C-C (PFA fixed) or full-length (center rod domain) LA/C-rod (PFA fixed). In addition, we used a polyclonal Ab pLA/C (MetOH fixed) (Figure 3). Finally, histone H3 and H3K9me3 Abs and fluorophore-conjugated phalloidin against F-actin were used as controls (Supplemental Figure 3).

The analyses of normalized intensity values (see Materials and Methods) showed that the total fluorescence intensity was increased due to the iterative staining with all tested Abs but not with the phalloidin (Figure 3, Supplemental Figure 3). For the lamin stained samples, the iterations increased the background-corrected mean fluorescence intensity of LA/C-N by ~2.7 fold in PFA-fixed (Figure 3A) and by ~3.6 fold in MetOH-fixed samples (Figure 3B). Similarly, the intensities were increased in PFA-fixed LA/C-C, LA/C-rod and MetOH-fixed pLA/C -stained samples by ~1.9 fold, ~4.4 fold, and ~8.6 fold, respectively (Figure 3C-F). Consequently, the background intensity (I_B) was increased by ~2.4 fold for PFA-fixed LA/C-N, by ~2.2 fold for MetOH-fixed LA/C-N, by ~2.5 fold for PFA-fixed LA/C-C, by ~7.4 fold for PFA-fixed LA/C-rod, and lastly, by ~8.6 fold for MetOH-fixed pLA/C (Figure 3A-F). However, even after four iterations, the background staining interfered neither with the detection nor the visual interpretation of the results with the studied Abs. This was apparent especially from the quantitated SBRs. Specifically, the mean background-corrected SBRs after the first iteration were ~28.80 for LA/C-N (PFA), ~31.42 for LA/C-N (MetOH), ~16.26 for LA/C-C (PFA), ~10.37 for LA/C-rod (PFA), and ~3.73 for pLA/C (MetOH) (Figure 3A-3E, right panels). To analyze and to compare the SBRs in the following iterations, the SBRs from the first iteration were normalized to 1. Next, the SBRs for the following iterations were calculated and normalized to iteration 1) (Figure 3A-3E, right panels). After the four iterations, the SBR in LA/C-N (PFA) staining was remained nearly unaltered (from 1 to 1.26, statistically non-significant, ns, $p>0.05$). In contrast, in MetOH fixed LA/C-N samples, the SBR was increased by each iteration and was significantly improved after the fourth iteration (from 1 to 1.7, ***$p<0.01$). For the LA/C-C (PFA), the SBR also remained nearly similar during the first three iterations but slightly decreased after the fourth (from 1 to 0.78, *$p<0.05$). In LA/C-rod (PFA) treated samples, the SBR was significantly lowered after the four iterations (from 1 to 0.592, ****$p<0.001$). This suggested that the polyclonal binding property of the Ab might have negatively affected the SBR during the iterations. Lastly, the SBR was well retained in four pLA/C (MetOH) iterations (remained as 1, ns, $p>0.05$). Notably, the IT-IF improved the intensities and SBRs of both histone Abs (H3 (PFA) and H3K9me3 (MetOH)) but did not affect phalloidin (PFA fixation) detection (Supplemental Figure 3). These analyses show that the iterations increase the intensity of the samples and maintain the SBR depending on the Ab

specificity. Thus, the absolute difference between the signal and background increased considerably. It was then sought to determine how the iterations affected the super-resolution imaging of the samples. To this end, SIM and ExM-LSCM imaging after the first and fourth iterations were done. The experiment showed that the iterations enabled SIM imaging with shorter exposure times as the sample intensity was increased. Also, the structural details, including the nuclear lamina at the nuclear rim, appeared more uniform (Figure 4A and 4B). Similarly, the ExM-LSCM imaging showed that the iterations seemed to increase the sample intensity, and notably, the lamin organization appeared more evident and visible (Figure 4C and 4D). These results indicated that iteration-enhanced labeling density within the sample leads to enhanced sample signal intensity and contrast.

Together, these results show that the IT-IF improves the sample imaging properties. Specifically, the signal intensity was increased without compromising the SBR. While using either low concentrations or low-affinity Abs might reduce background, it causes low signal intensity to be lost in noise.

IT-IF together with modelling -based denoising improves nuclear lamin network detection

Finally, we sought to determine whether the IT-IF improves the analysis of spatial organization i.e., composition of nuclear lamina. For this, we performed four iterations with LA/C-N by each time using a different fluorophore-conjugated 2°Abs on the same sample (Figure 5A-B). Alexa 647 2°Ab was used to detect the first and second iterations, and Alexa 568/Alexa 488 to detect the third and the fourth iteration, respectively (Figure 5A-B). This multicolor staining enabled the detection of the respective unique labeling patterns (Figure 5C) and analysis of their spatial correlations (Figure 5D).

The multicolor analysis of iterations 2-4 revealed that each iteration enhanced the occupancy of lamin Abs improving (Figure 5A and 5B). Specifically, the enhancement occurred by Ab binding to new targets not bound by preceding iterations. This was also deduced from the intensity line profile analysis showing color-unique peaks i(Figure 5C, n=2). Pearson´s correlation coefficient (PCC) analysis confirmed this result and indicated that while the correlation between the stainings was reasonably strong, it became significantly weaker between the consecutive iterations. Specifically, the PCC of the combined first and second stainings compared to the third was found to be 0.839 ± 0.037 and weakened to 0.794 ± 0.067 in comparison to that of the fourth iteration (**$p<0.01$, Student´s paired T-test, n=3) (Figure

5D). These results show that each consecutive staining produced new and additional binding along the lamins.

Finally, the properties of lamin network detection were compared in primary Ab concentration -enhanced (4X 1° Ab and 1X 2° Ab) and four times iterated LA/C-N –stained samples by using ExM. However, the images were noisy and required solutions for reliable network analyses. Due to the physical acquisition process of ExM, measured data often features a low signal-to-noise ratio. If any type of analysis must be performed on the data, it is reasonable to first process the noisy observation to get a faithful estimation of the clean signal from the acquired noisy data. For this purpose, we developed a signal-processing software for Noise Estimation, Denoising, and Deblurring [https://github.com/lucioazzari/NoiseEstimationDenoisingDeblurring] that automatically estimates the noise affecting the data and performs signal reconstruction intended as denoising plus deblurring (see Materials and Methods for detailed description for the pipeline). After processing the images of concentration-enhanced and four-time iterated samples, we observed a clear improvement in the overall signal quality showing well-defined lamin structures. Specifically, it enabled detailed quantitative analysis of the lamin network architecture and direct comparison of the labeling methods in detection of this network. The quantification of the lamin network architecture was done by using the Avizo 2020.2 software (Thermo Fisher Scientific, Waltham, MA, USA). First, the Auto Skeleton module was used to extract the centerlines from the network structures. Secondly, the formed graph was analyzed with the Spatial Graph Statistics module. In this quantification, the physical properties of the LA/C-N –stained lamin network were determined by first analyzing the lamin segment length and width. The analysis showed equal lamin segment length and radius for both 4X 1°Ab/1X 2°Ab and four times iterated samples (0.16±0.009 µm and 0.15±0.004 µm; and 0.06±0.00 µm and 0.06±0.00 µm, respectively) showing that the two different approaches did not affect the physical properties of the lamin segments (Figure 5E-G). The network properties were analyzed by quantifying the numbers of either total, terminating, and branching nodes connecting the lamin structures, and the number of lamin segments. Here, the analysis (n=2) indicated a significantly higher numbers of total and branching nodes in the pre-ExM treatment with four iterations (519 nodes, ***p=0.001; and 274 nodes, ***p<0.0001, 2way ANOVA multiple comparisons tests) in comparison to the concentration enhanced sample (449 total nodes and 181 branching nodes) (Figure 5H). There were no differences in the number of terminal nodes between the samples. In addition, the analysis indicated a significant (***p<0.00012way ANOVA multiple comparisons test) increase in the number of lamin

segments in the four times iterated sample (565 segments) in comparison to the concentration-enhanced sample (429 segments) (Figure 5H). Together, the results indicate that the iterative pre-ExM method improved the detection of nuclear lamina network.

Overall, the findings of this study indicate that IT-IF combined to ExM and signal processing is beneficial to the detection of nuclear lamin structure in the super-resolution scale, as it provides high labeling density, intensity, uncompromised SBR. Together with our signal processing pipeline, IT-IF enables a more complete quantitative analysis of nuclear lamina network organization. Beyond the nuclear lamina study presented here, we expect that our IT-IF method and signal processing platform can be useful in a wide range of nanoscopy applications.

Materials and methods

Cells and viruses

Madin-Darby canine kidney (MDCK) type IIG cells were maintained in low glucose MEM (#41090093, Thermo Fisher Scientific, Gibco™, Paisley, UK) supplemented with 1 % (vol/vol) penicillin-streptomycin antibiotics (#15140122, Thermo Fisher Scientific) and with 10% fetal bovine serum (#10500064, Thermo Fisher Scientific). Cells were maintained under standard 37 °C and humidified atmosphere with 5 % CO_2, passaged once a week. For the experiments, cells were seeded for seven days on collagen I (#A1064401, Thermo Fisher Scientific) coated cover glasses (18x18 mm for conventional laser scanning confocal microscopy (LSCM), 22x22mm for Expansion Microscopy, high performance, D=0.17 mm, Carl Zeiss Microscopy, NY, USA) prior fixation.

For ExM studies, Vero cells (ATCC) grown on glass coverslips in low-glucose DMEM GlutaMAX (with pyruvate, #11570586, Gibco, Thermo Fisher Scientific) to 90 % confluency and inoculated with herpes simplex virus 1 (HSV-1, MOI 5). The infected and noninfected cells were washed with phosphate-buffered saline (PBS) and fixed with 4 % PFA after 17 h post-infection (pi).

Antibodies

HSV-1 capsids were detected with HSV-1 VP5 MAb (sc-13525, Santa Cruz Biotechnology, Dallas, TX, USA). To detect A-type lamins in this study, mouse monoclonal Abs (mMAbs) against lamin A/C C-terminus residues aa 319-566 (LA/C-C, 131C3, ab1791, Abcam, Cambridge, UK) and lamin A/C N-terminus residues aa 2-29 (LA/C-N, E-1, sc-376248, Santa

Cruz Biotechnology, DA, USA), a rabbit monoclonal Ab (rMAb) against full-length lamin A/C (LA/C-rod, EP4520-16, ab133256, Abcam), and a rabbit polyclonal Ab (rpAb) against LA/C (exact target sequence declared as proprietary by the manufacturer, ab227176, Abcam) were used. To detect histone H3, a rpAb corresponding to the aa100 of the C-terminus (H3, ab1791, Abcam) was used. RpAb against H3 tail modification at N-terminal aa 1-100 tri-methyl lysine 9 (H3K9me3, Abcam) and anti-actin fluorophore-conjugated phalloidin (ATTO-TEC, NY, USA) were applied in supplemental studies.

Iterative immunostaining

MDCKII cells were fixed with 4 % paraformaldehyde (cat. No. 15713-S, Electron Microscopy Sciences, Hatfield, PA, USA) for 10 min at room temperature (RT), rinsed twice with 1X PBS, and permeabilized for 10 min in RT using 0.5 % Triton X-100 in PBS supplemented with 0.5 % BSA (Bovine Serum Albumin). Iterative immunostaining was begun by incubating the samples with primary Abs diluted in 3 % bovine serum albumin (BSA) for 1h in RT using recommended immunofluorescence labeling working concentrations. Next, the primary Abs (see Table 1) were followed by secondary Alexa 488 and Alexa 568 -conjugated goat anti-mouse and anti-rabbit Abs (1:200 in 3 % BSA/PBS, Thermo Fisher Scientific, Waltham, MA, USA), respectively, for 1h in RT in the dark. This protocol was repeated three times to iterate the Ab treatment and signal intensity. Prior to each subsequent iteration, the permeabilization step was done using 0.2 % Triton X-100 in PBS supplemented with 0.5 % BSA. After the four iterations, the samples were washed with PBS and deionized water (10 min each) followed by mounting in ProLong Diamond Antifade Mountant with DAPI (Thermo Fisher Scientific) and led to cure at RT in dark o/n before storing at +4 °C prior to microscopy.

For the expansion of iteratively immunostained samples, a fourfold concentration of secondary Abs was used to retain the signal after expansion. Sample expansion was performed using the previously described proExM protocol for cultured cells (V1.0, REF). After the isotropic expansion, a piece of gel was gut and mounted with 1 % high-melt agarose into an imaging chamber (SC15022, AirekaCells, Hong Kong, China).

Expansion microscopy

The samples going through expansion protocol were first fixed and stained according to the iterative immunostaining protocol described previously. After the immunolabeling, the samples were incubated in an anchoring solution of 1% 6-((acryloyl)amino) hexanoic Acid, Succinimidyl Ester (#A20770, Acroloyl X-SE, Thermo Fisher Scientific) in PBS for over 6

hours in RT. After the anchoring, the samples were washed with PBS for 2 x 15 mins before proceeding to gelation. Before the gelation, glass coverslips (18mm x 18mm) were prepared to work as a base to cast the gel. A piece of parafilm (P7793, Merck, NJ, USA) was glued on top of a coverslip with a drop of cyanoacrylate glue (Loctite Super Glue Power Flex Gel Control, Henkel Norden AB, Bromma, Sweden). The parafilm-coated coverslip was then placed on a 6-well plate lid, parafilm side on top, and the parafilm cover paper was removed. Then, an in-house designed 3D printed spacer was placed on top of the parafilm. The purpose of the spacer is to confine the gel to known dimensions and keep the thickness of the gel as thin as possible. These features will help define the expansion factor and the expansion speed of the gel.

The gelation solution was prepared on ice by adding the inhibitor (4-Hydroxytempo) and the accelerator (TEMED) to the monomer solution. The initiator (APS) was added to the solution just before pipetting it into the opening of the spacer as the solution will gelatinize fast after the inclusion of APS. Thus, it is advisable to prepare the solution into aliquots to separate 1,5ml centrifuge tubes (S1615-5500, Starlab International, Hamburg, Germany) for one to two samples at a time. After adding APS, the solution was vortexed and administered in the middle of the open space in the spacer. Then, the sample was placed carefully on top of the gelling solution sample-side towards the gel. A channel in the spacer ensures that excess gelling solution will flow out. A metal nut was placed on the constructed gel mold to provide extra weight. The sample was left to polymerize for 30-45 mins in RT.

After the gel had polymerized, the parafilm-coated coverslip was removed carefully. The gel will not stick to the parafilm, and it is straightforward to remove it. A scalpel can be used to trim excess gel from the edges of the gel button. With the sample coverslip still attached, the gel was placed on a clean 6-well plate (#150239, Thermo-Fisher Scientific). Only one sample was placed in one well. It is essential to measure and draw the outlines of the gel button at this time because the gel will start swelling during digestion. It is crucial to know the original size of the gel button when defining the final expansion factor for the sample. We are using custom-made spacers with a well-defined area for the gel button. Thus, it will be the same size every time.

The polymerized gel, together with the sample, was immersed in a 10-fold volume of digestion solution consisting of Tris pH 8.0, EDTA (E5134, Merck, NJ, USA), Triton X-100 (T8787, Merck), guanidine HCl (G3272, Merck), and Proteinase K (P8107S, New England Biolabs, Ipswich, USA). The sample was incubated in the solution overnight at room temperature and dark. The gel will detach from the coverslip during incubation or, at the latest, during the first wash with double-distilled water (ddH_2O). The detached gel was moved to a 6-

cm dish preserving the orientation of the gel. It is essential to know the side which includes the sample due to the vast size increase of the sample during the next step. The gel was washed with an excess volume of ddH_2O for 1 hour, 3-5 times. The hydrophilic gel will swell during these washes until the expansion reaches a plateau after the third or fourth wash.

Finally, the expanded gel sample was measured for the expansion factor (final dimensions/ original dimensions). The gel was cut with a custom-made puncher, and the resulting gel disc was mounted in a live imaging chamber (AirekaCells) with low-melt agarose (A7431, Merck). The chamber was filled with ddH_2O to prevent sample shrinkage and drying

Confocal Microscopy

For LSCM, all samples were prepared as two replicates (n=2) and imaged using constant laser powers and detection voltages, enabling comparable quantitative analysis of the fluorescence intensities. At the confocal microscope, Alexa 488 and Alexa 568 were excited with 488 nm and 561 nm solid-state lasers, respectively. Fluorescence was detected with 525/50 nm and 595/50 band-pass filters. For unexpanded samples, Nikon Apo 60x Oil λS DIC N2, numerical aperture (N.A.) 1.40, the working distance (WD) 0.14 mm was used in imaging, and stacks of 1024x1024 pixels were collected with a pixel size of 0.041-0.052, or 104 nm in the x- and y -directions and 150 nm in the z-direction. For expansion microscopy sample imaging, Nikon CFI Plan Apo IR SR 60x WI, N.A. 1.27, WD 0.17 mm objective was used. Stacks of 1024x1024 pixels were collected with a pixel size of XX nm in the x- and y- directions and 180 nm in the z-direction. The imaging was done using constant laser powers and detection voltages, enabling a comparative analysis of the fluorescent intensity in each channel. Image analysis was done with FIJI (Schindelin *et al.*, 2012) (REF).

Analysis of nuclear lamin intensity and data normalization

After imaging, the mean fluorescence intensity of the nuclear lamina (measured from the total segmented nuclear area) and the background staining intensity (image area omitting the segmented nuclei) were measured. Additionally, detector noise background correction was imaged from similarly mounted samples containing fluorescent beads (from the area omitting the beads). The detector background was then subtracted from the measured values (background correction), and the background-corrected intensity value was normalized to the starting mean intensity value obtained from iteration 1.

Signal processing pipeline for noise estimation, denoising and deblurring

In our model for confocal microscopy data, we assume the noise to be additive with signal-dependent variance and spatially correlated (Azzari, Borges and Foi, 2018). The signal-dependent variance models the conversion of light into electric charge and the dark thermal noise. Specifically, the noise variance is an affine function of the signal-expectation (Foi *et al.*, 2008). The noise correlation models the system's optics and the light's diffraction pattern, commonly referred to as point spread function (PSF), after passing through the microscope's lenses (Cole, Jinadasa and Brown, 2011). We model correlated noise as the convolution between a kernel and a white Gaussian random field. Alternatively, noise correlation can be modeled with the noise power spectral density (PSD), that is the distribution of the noise energy (or variance) in Fourier domain. Kernel and PSD are related to each other; in particular, the kernel can be calculated as the inverse Fourier transform of square root of the noise the PSD. In our noise model, the noise correlation happens before the sensor converts the photons into current; thus, we consider the case of signal-dependent noise post correlation (Azzari, Borges and Foi, 2018)(See Eq. (53). In our processing pipeline we first estimate, modulo a scaling factor, the noise variance function; this is done using the algorithm (Foi *et al.*, 2008). This algorithm is designed for estimating the variance function of signal-dependent white noise and when the noise is spatially correlated (i.e., not white), the algorithm's output is off by a scaling factor that depends on the correlation (Azzari, Borges and Foi, 2018)(See Eq. (68)), which must be estimated separately. To identify this factor, we exploit the fact that the noise spatial correlation does not affect the statistics of an individual pixel (e.g., the variance of a pixel corresponds exactly to a point of the noise variance function). First, we estimate mean and variance of non-overlapping 1x1x8 windows (i.e., only in the axial direction) of the 3D sequence; we discard the first and last quartiles of the measured variances to remove possible outliers; then we fit a second affine mean-variance function over the remaining points, and we compare the variances from the two affine models at the intensity value of the mean of the observed image: we correct the first function with the ratio between the two values. Next, the noise function is used to apply the generalized Anscombe transform (GAT) (Starck, Murtagh and Bijaoui, 1998) to our data. The GAT is a variance stabilizing transformation of noisy data that makes the noise variance independent of the signal. In this way we can estimate the noise PSD using, indiscriminately, the whole stabilized data. For practical reasons it is convenient to estimate the PSD in discrete cosine transform (DCT) domain on a small support 8x8, and then to convert it to the actual noise PSD (Azzari, Borges and Foi, 2018; see Eq. (77)). To estimate the PSD DCT 8x8 we first divide the whole sequence in 3D overlapping 8x8x8 cubes; then,

for each cube, we first compute the 2D DCT of each 2D spatial plane, and then we apply, coefficient-wise, the squared median of absolute deviation (multiplied by 1.4826) in the axial direction: in this way we obtain a set of 2D estimates of the 2D noise PSD DCT 8x8, one for each group. Because some estimates might be affected by outliers, we discard some of the estimates. Finally, we estimate the final noise 2D PSD DCT 8x8 by applying the sample median coefficient-wise to all the remaining PSD estimates. Because the noise has been stabilized and a PSD estimate is now available, we can apply any of the many off-the-shelf denoising algorithms developed for correlated additive Gaussian noise to denoise our data.

We denoised the sequence using the framework introduced in (Azzari and Foi, 2016). This approach iteratively filters and refines the estimation in a multi-scale fashion, from coarse to fine scale: at each scale it first performs binning of the data, and then it applies VST. The resulting signal is corrupted by additive signal-independent correlated noise that can be denoised with any algorithm designed for correlated noise. This iterative approach is well suited for data affected by strong noise (such is the case of expansion microscopy), and it ensures state-of-the-art denoising results. The denoising filter that we use within the framework is the RF3D algorithm (Maggioni, Sánchez-Monge and Foi, 2014), that is designed for videos (3D data) corrupted by correlated noise. It is important to remark that RF3D performs well in challenging cases such as 3D expansion microscopy because it exploits the redundant spatial and temporal information by promoting sparsity of small 3D spatio-temporal volumes. The software allows the user to also perform deconvolution (deblurring) of the denoised sequence. However, the results reported in the analysis above have not been deconvolved.

SIM

Nikon N-SIM system in Nikon Ti-E inverted microscope body with CFI SR Apochromat100x/1.49 oil immersion objective and Andor iXon Ultra 897 was used for super-resolution SIM imaging. The spherical aberration correction was conducted before every imaging session by using subresolution fluorescent beads (PS-Speck, Thermo Fisher Scientific). This was followed by illumination pattern alignment and optimization for the used laser lines (488nm, 561nm and 640nm). Alexa 488 and Alexa 568 were excited with 488 nm and 561 nm solid-state lasers, respectively. The SIM image reconstruction was conducted in the system by using NIS-elements software.

ExM lamin network analysis

ExM image stacks from the 1x and 4x iterations were used to analyze the stained lamin network coverage. Overall, three areas per sample were analyzed from two samples per iteration. For this purpose, the image stacks were first divided into two sub-stacks, apical and basal. The apical sub stack was used for the final analysis. First, the stack was normalized, and a ridge detection algorithm (Steger, 1998; Wagner, Hiner and xraynaud, 2017) was used to detect string-like lamin a/c structures. The following thresholded image stacks were analyzed by making a maximum intensity projection for area coverage, and by analyzing the network in Avizo 2020.2 (Thermo Fisher Scientific, Waltham, USA) for nodal and branch length analysis. First, the Auto Skeleton module was used to extract the centerlines from the network structures. Secondly, the formed graph was analyzed with the Spatial Graph Statistics module.

Acknowledgements

This work was supported by the Academy of Finland under the award numbers 308315 and 314106 (TOI), 330896 (MVR), 332615 (EM), and the Centre of Excellence in Body-on-Chip Research (312412 (JH)), 336357 (PROFI6 - TAU Imaging Research Platform (LA, MV, AF), and by the Jane and Aatos Erkko Foundation (MVR). University of Jyväskylä Graduate School for Doctoral Studies is acknowledged for the support (SM). The authors acknowledge Biocenter Finland, and Tampere University Tampere Imaging Facility, Virus Production Facility (Title of Docent Eric Dufour), and Flow Cytometry Facility (Dr. Laura Kummola) for their services.

References

Ankam S, Teo BKK, Pohan G, Ho SWL, Lim CK, Yim EKF (2018). Temporal changes in nucleus morphology, lamin A/C and histone methylation during nanotopography-induced neuronal differentiation of stem cells. *Front Bioeng Biotechnol* May 31, 6:69, doi: 10.3389/fbioe.2018.00069.

Azzari L, Borges LR, Foi A. 2018. Modeling and estimation of signal-dependent and correlated noise. In: Denoising of photographic images and video: fundamentals, open challenges and new trendsed (Advances in Computer Vision and Pattern Recognition), ed. M. Bertalmío. Springer International Publishing, doi: 10.1007/978-3-319-96029-6_1, 1–36.

Azzari L, Foi A. 2016. Variance stabilization for noisy+estimate combination in iterative poisson denoising. *IEEE Signal Process Lett* 23:8, 1086–1090, doi: 10.1109/LSP.2016.2580600.

Baines JD. 2011. Herpes simplex virus capsid assembly and DNA packaging: A present and future antiviral drug target. *Trends Microbiol* 19:12, 606–613, doi: 10.1016/j.tim.2011.09.001.

Brueckner L, Zhao PA, van Schaik T, Leemans C, Sima J, Peric-Hupkes D, Gilbert DM, van Steensel B. 2020. Local rewiring of genome–nuclear lamina interactions by transcription. *EMBO J* 39:6, 1–17, doi: 10.15252/embj.2019103159.

Cavalli G, Misteli T. 2013. Functional implications of genome topology. *Nat Struct Mol Biol* 20:3, 290–299, doi: 10.1038/nsmb.2474.

Chen J, Sasaki H, Lai H, Su Y, Liu J, Wu Y, Zhovmer A, Combs CA, Rey-Suarez I, Chang H-Y, et al. 2021. Three-dimensional residual channel attention networks denoise and sharpen fluorescence microscopy image volumes. *Nat Methods* 18:6, 678–687, doi: 10.1038/s41592-021-01155-x.

Cole RW, Jinadasa T, Brown CM. 2011. Measuring and interpreting point spread functions to determine confocal microscope resolution and ensure quality control. *Nat Protocols*, 6:12, 1929–1941, doi: 10.1038/nprot.2011.407.

Dahl, KN, Kahn SM, Wilson KL, Discher DE. 2004. The nuclear envelope lamina network has elasticity and a compressibility limit suggestive of a molecular shock absorber. *J Cell Sci* 117:20, 4779–4786, doi: 10.1242/jcs.01357.

Dankovich TM, Rizzoli SO. 2021. Challenges facing quantitative large-scale optical super-resolution, and some simple solutions. *iScience* 24:3, 102134, doi: https://doi.org/10.1016/j.isci.2021.102134.

Dixon JR, Jung I, Selvaraj S, Shen Y, Antosiewicz-Bourget JE, Lee AY, Ye Z, Kim A, Rajagopal N, Xie W, *et al.* 2015. Chromatin architecture reorganization during stem cell differentiation. *Nature* 518:7539, 331–336, doi: 10.1038/nature14222.

Figueiras E, Silvestre OF, Ihalainen TO, Nieder JB. 2019. Phasor-assisted nanoscopy reveals differences in the spatial organization of major nuclear lamina proteins. *Biochim Biophys Acta Mol Cell Res* 1866:12, 118530, doi: 10.1016/j.bbamcr.2019.118530.

Foi A, Trimeche M, Katkovnik V, Egiazarian K. 2008. Practical poissonian-gaussian noise modeling and fitting for single-image raw-data. *IEEE Trans Image Process* 17:10, 1737–1754, doi: 10.1109/TIP.2008.2001399.

Fortin JP, Hansen KD. 2015. Reconstructing A/B compartments as revealed by Hi-C using long-range correlations in epigenetic data. *Gen Biol* 16:1, 1–23, doi: 10.1186/s13059-015-0741-y.

Gao R, Yu CC (J), Gao L, Piatkevich KD, Neve RL, Munro JB, Upadhyayula S, Boyden ES. 2021. A highly homogeneous polymer composed of tetrahedron-like monomers for high-isotropy expansion microscopy. *Nat Nanotech* 16:6, 698–707, doi: 10.1038/s41565-021-00875-7.

Gaudreau-Lapierre A, Mulatz K, Béïque JC, Trinkle-Mulcahy L. 2021. Expansion microscopy-based imaging of nuclear structures in cultured cells. *STAR Protocols* 2:3, 100630, doi: https://doi.org/10.1016/j.xpro.2021.100630.

Ikoma H, Broxton M, Kudo T, Wetzstein G. 2018. A convex 3D deconvolution algorithm for low photon count fluorescence imaging. *Sci Rep* 8:1, 11489, doi: 10.1038/s41598-018-29768-x.

Laine RF, Albecka A, van de Linde S, Rees EJ, Crump CM, Kaminski CF. 2015. Structural analysis of herpes simplex virus by optical super-resolution imaging. *Nat Commun* 6:1, 5980, doi: 10.1038/ncomms6980.

Lau L, Lee YL, Sahl SJ, Stearns T, Moerner WE. 2012. STED microscopy with optimized labeling density reveals 9-fold arrangement of a centriole protein. *Biophys J* 102:12, 2926–2935, doi: https://doi.org/10.1016/j.bpj.2012.05.015.

Maggioni M, Sánchez-Monge E, Foi A. 2014. Joint removal of random and fixed-pattern noise through spatiotemporal video filtering', *IEEE Trans Image Process* 23:10, 4282–4296, doi: 10.1109/TIP.2014.2345261.

Newcomb WW, Homa FL, Thomsen DR, Booy FP, Trus BL, Steven AC, Spencer JV, Brown JC. 1996. Assembly of the herpes simplex virus capsid: Characterization of intermediates observed during cell-free capsid formation. *J Mol Biol* 263:3, 432–446, doi: 10.1006/jmbi.1996.0587.

Ojala PM, Sodeik B, Ebersold MW, Kutay U, Helenius A. 2000. Herpes simplex virus type 1 entry into host cells: reconstitution of capsid binding and uncoating at the nuclear pore complex in vitro. *Mol Cell Biol* 20:13, 4922–4931, doi: 10.1128/mcb.20.13.4922-4931.2000.

Pawley JB. 2006. *Handbook Of Biological Confocal Microscopy*, *Handbook Of Biological Confocal Microscopy*, ed. J. B. Pawley, Boston, MA, Springer US, doi: 10.1007/978-0-387-45524-2.

Robson MI, de Las Heras JI, Czapiewski R, Thành PL, Booth DG, Kelly DA, Webb S, Kerr ARW, Schirmer EC. 2016. Tissue-specific gene repositioning by muscle nuclear membrane proteins enhances repression of critical developmental genes during myogenesis. *Mol Cell* 62:6, 834–847, doi: 10.1016/j.molcel.2016.04.035.

Schindelin J, Arganda-Carreras I, Frise E, Kaynig V, Longair M, Pietzsch T, Preibisch S, Rueden C, Saalfeld S, Schmid B. 2012. Fiji: an open-source platform for biological-image analysis. *Nat Methods* 9:7, 676–682; doi: 10.1038/nmeth.2019.

Schirmer EC, Florens L, Guan T, Yates 3rd JR, Gerace L. 2003. Nuclear membrane proteins with potential disease links found by subtractive proteomics. *Science* 301:5638, 1380–1382, doi: 10.1126/science.1088176.

Schnell U, Dijk F, Sjollema KA, Giepmans *BNG.* 2012. Immunolabeling artifacts and the need for live-cell imaging. *Nat Methods* 9:2, 152–158, doi: 10.1038/nmeth.1855.

Starck J-L, Murtagh FD, Bijaoui A. 1998. *Image processing and data analysis: The multiscale approach*. Cambridge, Cambridge University Press, doi: DOI: 10.1017/CBO9780511564352.

Steger C. 1998. An unbiased detector of curvilinear structures. *IEEE Trans Pattern Anal Mach* 20:2, 113–125, doi: 10.1109/34.659930.

Tillberg PW, Chen F, Piatkevich KD, Zhao Y, Yu C-C (J), English BP, Gao L, Martorell A, Suk H-J, Yoshida F. 2016. Protein-retention expansion microscopy of cells and tissues labeled

using standard fluorescent proteins and antibodies. *Nat Biotech* 34, 987–992, doi: 10.1038/nbt.3625.

Truckenbrodt S, Maidorn M, Crzan D, Wildhagen H, Kabatas S, Rizzoli SO. 2018. X10 expansion microscopy enables 25-nm resolution on conventional microscopes. *EMBO Rep,* 19:9, e45836, doi: https://doi.org/10.15252/embr.201845836.

Truckenbrodt S, Sommer C, Rizzoli SO, Danzl JG. 2019. A practical guide to optimization in X10 expansion microscopy. *Nat Protocols* 14:3, 832–863, doi: 10.1038/s41596-018-0117-3.

Turgay Y, Eibauer M, Goldman AE, Shimi T, Khayat M, Ben-Harush K, Dubrovsky-Gaupp A, Sapra KT, Goldman RD, Medalia O. 2017. The molecular architecture of lamins in somatic cells. *Nature* 543:7644, 261–264, doi: 10.1038/nature21382.

Wagner T, Hiner M, xraynaud . 2017. 'thorstenwagner/ij-ridgedetection: Ridge Detection 1.4.0', doi: 10.5281/ZENODO.845874.

Wassie AT, Zhao Y, Boyden ES. 2019. 'Expansion microscopy: principles and uses in biological research. *Nat Methods* 16:1, 33–41, doi: 10.1038/s41592-018-0219-4.

Whelan DR, Bell TDM. 2015. Image artifacts in single molecule localization microscopy: Why optimization of sample preparation protocols matters. *Sci Rep* 5, 7924, doi: 10.1038/srep07924.

Figures and Figure Legends

Figure 1.

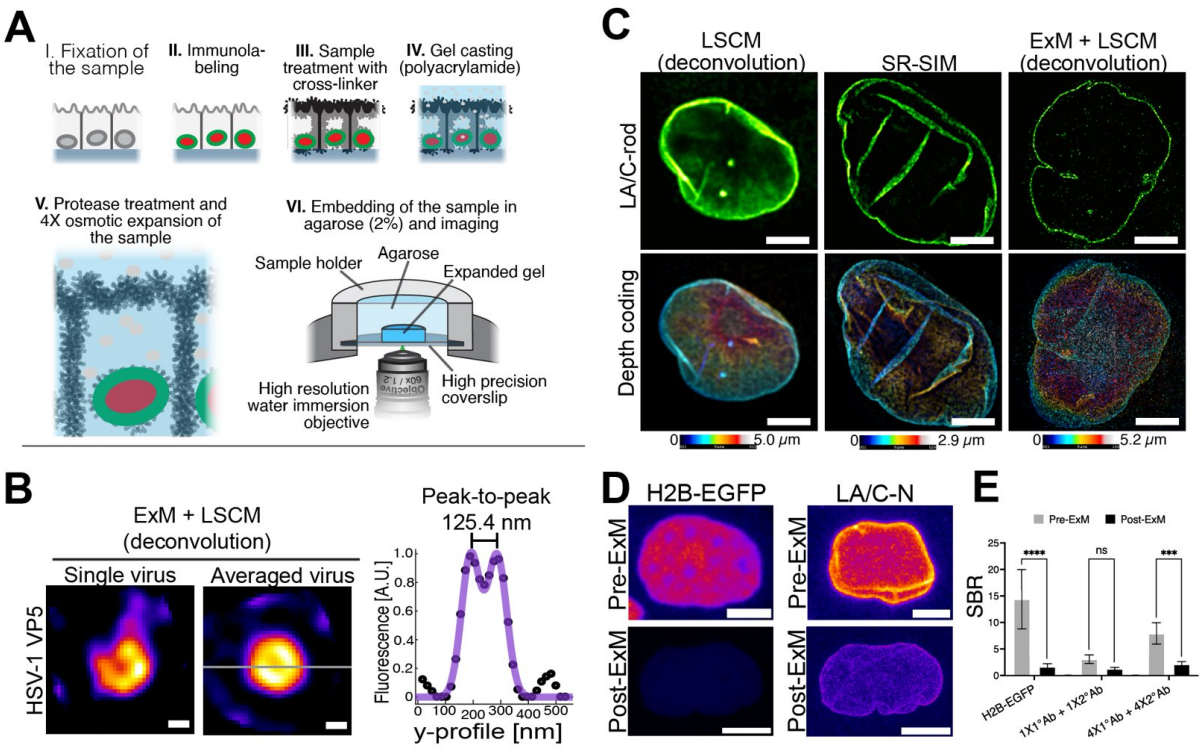

Figure 1. Graphical presentation of pre-expansion microscopy (pre-ExM) sample preparation method and influence of ExM on detection of intranuclear protein complexes and signal fluorescence intensity. (A) Schematics of pre-ExM sample preparation method and imaging setup showing critical steps of sample fixation (i), immunostaining (ii), Acroloyl-X crosslinking (iv), protease treatment followed by the osmotic ~4X expansion (v) and finally, mounting of the gel sample into an IREKA Cell for inverted laser scanning confocal microscopy (LSCM) using a high-resolution water immersion objective (vi). (B) Representative deconvoluted post-ExM confocal microscopy images of intranuclear single (left) and an averaged (n=6; right) viral protein 5 (VP5) Ab -stained HSV-1 nucleocapsids and the mean fitted capsid diameter (125.4 nm) measured as a peak-to-peak distance from the fluorescence histogram proving the symmetric expansion of even a complex nucleoplasmic protein complex. Scale bars, XX nm. (C) Deconvoluted LSCM (upper right), super-resolution structured illumination microscopy (SR-SIM) (upper middle), and deconvoluted ExM+LSCM images of an epithelial cell nucleus stained with a rod-domain targeting lamin A/C Ab (Ab) and depth-coded pseudo-color fluorescence intensity maps (lower panels) showing the effect on the detection resolution and proving the power of ExM in imaging of nuclear substructures. Scale bars, XX nm. (D) Representative pseudo-color fluorescence intensity indicator color

schemed pre-ExM (upper panel) and post-ExM (lower panel) LSCM images of endogenously expressed H2B-EGFP and LA/C-N -stained epithelial cell nuclei showing the decrease in fluorescence intensity after the ExM method. Scale bars, 5μm. (E) Quantification of the signal-to-background ratio (SBR) for H2B-EGFP, and LA/C-N staining before and after ExM with conventional 1X (left two columns) or enhanced 4X (middle two columns) concentrations of both primary (1°) and secondary (2°) Abs after LSCM imaging presenting the decrease in SBR following the ExM method. Columns represent the measured values as a mean ± standard deviation (SD).

Figure 2.

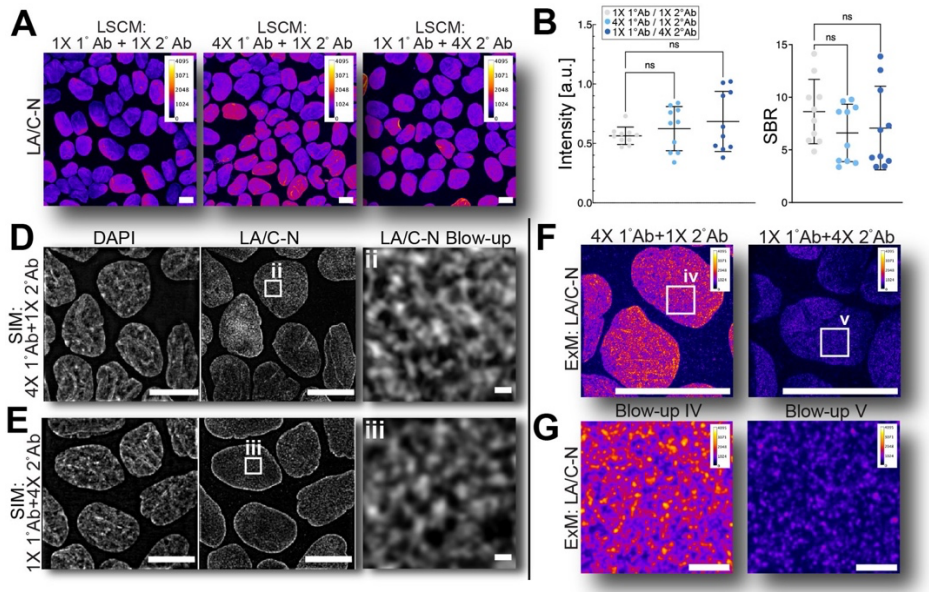

Figure 2. Effects of enhanced primary and secondary Ab concentration on target detection. (A) Representative pseudo-colored intensity indicator color-coded field LSCM images of LA/C-N-stained epithelial nuclei using either conventional 1X primary (1X 1°Ab) with 1X secondary (1X 2°Ab) concentration (left panel), 4-times enhanced primary Ab concentration (4X 1°Ab with 1X 2°Ab, middle panel), or 4-times enhanced secondary Ab concentration (1X 1°Ab with 4X 2°Ab, right panel). Scale bars, 10 µm. (B) Quantification of the mean LA/C-N fluorescence intensity in applied combinations of Ab concentrations (mean ± SD). (C) Quantification of signal-to-background ratio (SBR) in respective conditions (mean ± SD). Structured illumination microscopy (SIM) maximum intensity projection images and their respective blow-ups (ii and iii) of LA/C-N detection using (D) 4-times enhanced primary Ab concentration (4X 1°Ab with 1X 2°Ab, upper panels) and (E) 4-times enhanced secondary Ab concentration (1X 1°Ab with 4X 2°Ab, lower panels). Scale bars, 20 µm; blow-up scale bars, 1 µm. (F) Representative expansion microscopy (ExM) LSCM pseudo-color intensity indicator color-schemed maximum intensity projection images (upper panels; scale bars, 20 µm) and their respective blow-ups (iv and v; lower panels; scale bars, 1 µm) of 4-times enhanced primary Ab concentration (4X 1°Ab with 1X 2°Ab) and (G) 4-times enhanced secondary Ab concentration (1X 1°Ab with 4X 2°Ab). Experimental replicates n=2. Ordinary One-way ANOVA was used to test the statistical significance. Statistically non-significant (ns).

Figure 3.

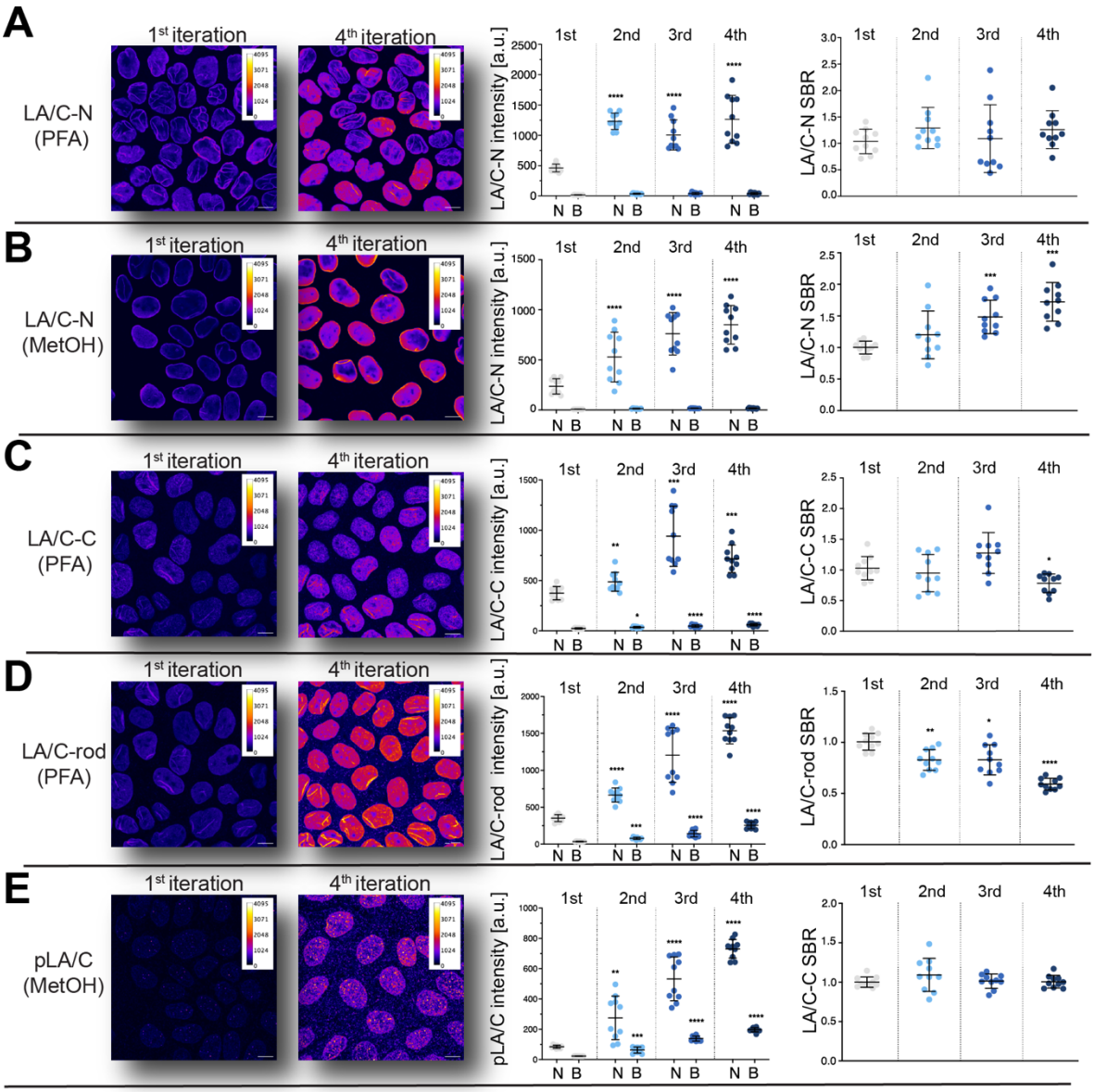

F

	Nuclear fluorescence intensity (mean ± SD)		Background fluorescence intensity (mean ± SD)	
Staining	**1st iteration**	**4th iteration**	**1st iteration**	**4th iteration**
LA/C-N (PFA)	462 ± 64	1264 ± 394	17 ± 4.0	39 ± 16
LA/C-N (MetOH)	236 ± 76	850 ± 193	8 ± 0.4	17 ± 5.0
LA/C-C (PFA)	377 ± 67	716 ± 138	24 ± 6.0	60 ± 12
LA/C-rod (PFA)	352 ± 46	1536 ± 177	34 ± 6.0	255 ± 46
pLA/C (MetOH)	85 ± 10	731 ± 62	23 ± 1.0	197 ± 14

Figure 3. Effect of iterative immunostaining on fluorescence signal intensity and detection quality of nuclear lamins. Representative pseudo-colored intensity indicator color-coded maximum intensity projections of LSCM images acquired after one (far left panels) or four (left panels) iterations i.e., consequent immunostaining cycles, and their respective quantifications of background-corrected mean fluorescence intensity (middle right panels), and

background-corrected signal-to-background ratio (SBR, normalized to iteration 1, far right panels) of (A) LA/C-N on PFA-, (B) LA/C-N on MetOH-, (C) LA/C-C on PFA , (D) LA/C-rod on PFA-, and (E) pLA/C on MetOH-fixed cells. Scale bars, 10 µm. F) Table containing the exact values from the above measurements of nuclear and background fluorescence intensities. Values in plots presented as a mean ± SD. Experimental replicates n=2. 2way ANOVA with multiple comparisons was used to test the statistical significance. Statistically non-significant (ns) $p>0.05$, *$p<0.05$, **$p<0.01$, ***$p<0.001$, ***$p<0.0001$.

Figure 4.

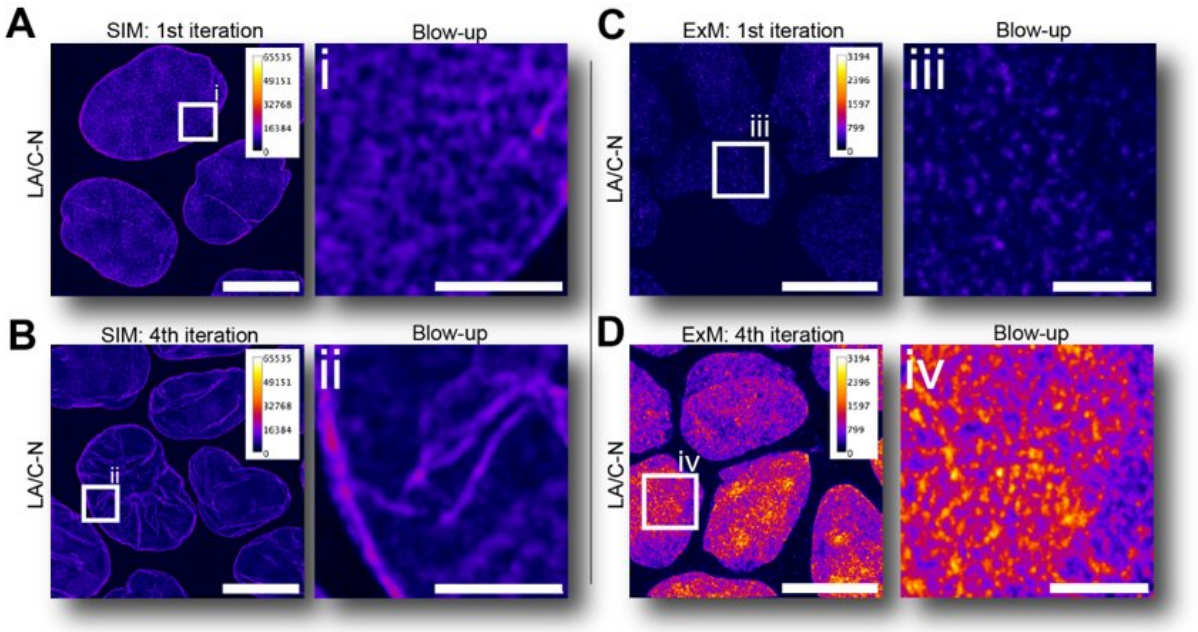

Figure 4. Super-resolution SIM imaging of IT-IF samples. SIM images of representative pseudo-colored intensity indicator color-coded maximum intensity projections and their blow-ups from indicated areas (white box) of (A) first (1st) and (B) four times iterated (4th) LA/C-N staining showing near equal intensities but improved features after 4th iteration. ExM-LSCM images of representative pseudo-colored intensity indicator color-coded maximum intensity projections and their blow-ups from indicated areas (white box) of (C) first (1st) and (D) four times iterated (4th) LA/C-N staining showing increased intensity and staining in the 4th iteration in comparison to those in 1st iteration. Scale bars, 10 µm, blow-up-scale bars, 2 µm), expansion factor of 4.4.

Figure 5.

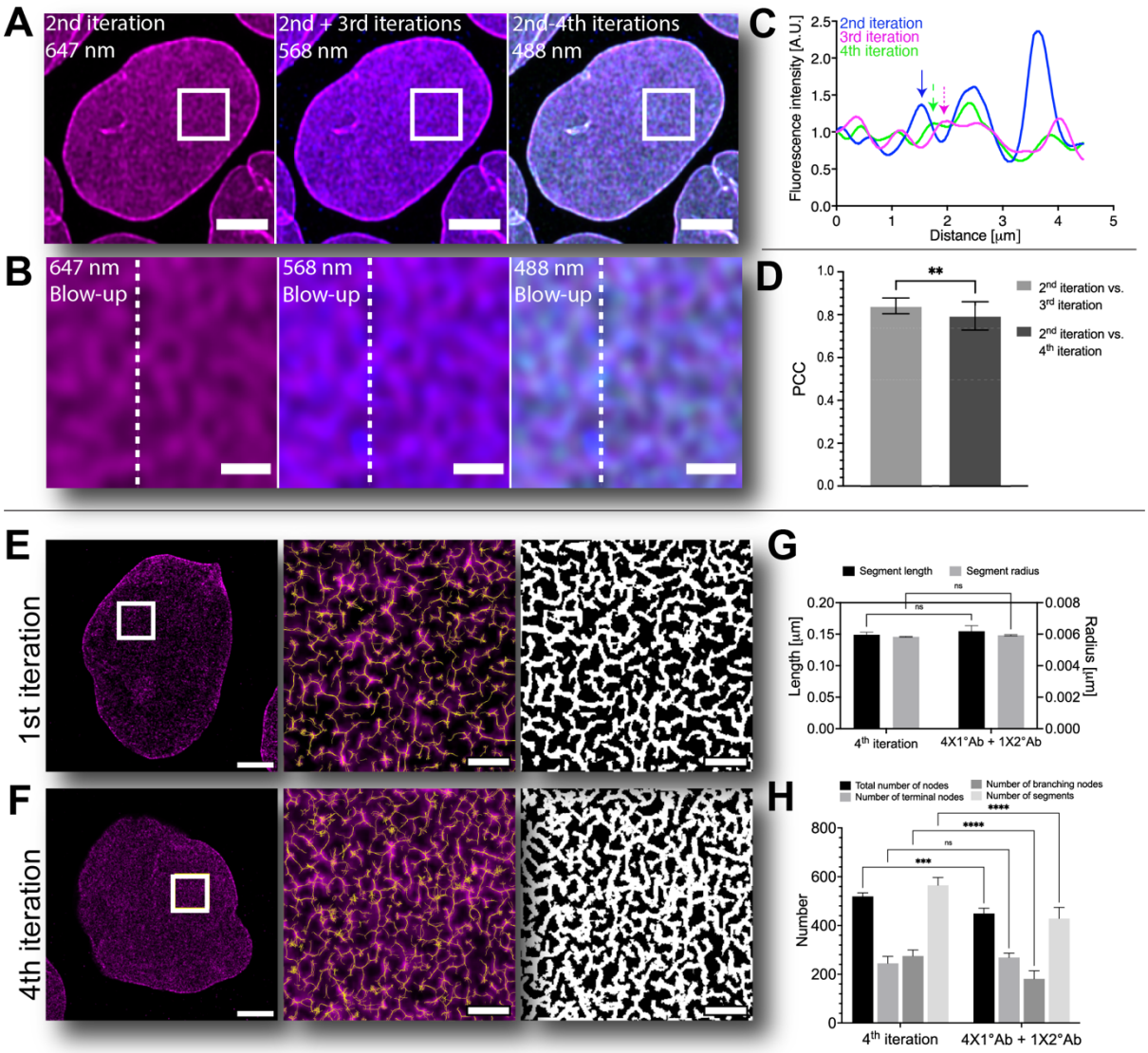

Figure 5. Nuclear lamina network architecture visualized by IT-IF combined with modelling -based denoising. (A) Representative LSCM single optical section images of multicolor analysis of LA/C-N iteration showing detection result after the first two iterations (Alexa 647, upper left panel, magenta), after 3rd (Alexa 568, upper middle panel, blue), and 4th iteration (Alexa 488, upper right panel, green). Scale bars, 5 µm. (B) Blow-ups of indicated areas shown in A. Scale bars, 1 µm. (C) Fluorescence intensity line profile analysis of areas indicated in B, showing fluorescence intensity distribution of combined 1st and 2nd. (magenta), 3rd (blue) and 4th iterations (green) showing increased Ab binding as iteration-specific intensity peaks. Sources of intensity resulting from unique iterations are represented with distinct arrows with respective colors (magenta: combined 1st and 2nd iterations; blue: 3rd iteration; green: 4th iteration). (D) Quantification of Pearson Correlation Coefficient (PCC) between indicated iterations. **p<0.01, Two-way ANOVA). Representative denoised ExM images of single

nuclei showing (E) ExM optimized LA/C-N staining using 4X 1°Ab/1X 2°Ab concentrations or (F) four times iterated LA/C-N (left panels, scale bars 3 µm), blow-out overlay of indicated areas (white boxes) with calculated network structure (yellow) containing nodes and segments obtained after the image analysis (middle panels, scale bars 500 nm) and reconstructed LA/C-N network (right panels, scale bars 500 nm). (G) Quantification of lamin segment physical properties. (H) Quantification of nuclear lamina architecture by presenting the number of total, branching, and terminating nodes as well as number of lamin segments within the network coverage. 2way ANOVA was used for statistical testing. Statistically non-significant (ns), p ***p<0.001, ***p<0.0001.